Supporting information for

P1 center network in high-pressure high-temperature diamonds is a readily accessible source of nuclear hyperpolarization at 14 T

Quentin Stern,[1] Jinlei Cui,[1] Raj Chaklashiya,[1,2] Celeste Tobar,[1,3] Martyna Judd,[1,4] Orit Nir-Arad,[5] Daphna Shimon,[6] Ilia Kaminker,[5] Hiroki Takahashi,[7] Jagadishwar R. Sirigiri,[8] & Songi Han[1,2†]

[1] Department of Chemistry, Northwestern University, 633 Clark Street, Evanston, 60208, IL, USA.
[2] Materials Department, University of California, Santa Barbara, 93106, CA, USA
[3] Department of Chemistry and Biochemistry, University of California, Santa Barbara, 93106, CA, USA.
[4] Research School of Chemistry, The Australian National University Canberra, ACT 2605, Australia.
[5] School of Chemistry, Tel-Aviv University, 6997801 Tel-Aviv, Israel.
[6] Institute of Chemistry, Hebrew University of Jerusalem, Jerusalem 9190401, Israel.
[7] JEOL Ltd., Akishima, Tokyo, 196-8558, Japan.
[8] Bridge12 Technologies, Inc., Natick, MA, USA.

[†] Correspondence: songi.han@northwestern.edu

Contents

1. Instrumentation

a. Ultra-low temperature MAS-NMR

We used a ULT MAS-NMR setup operating from room temperature down to 35 K using helium gas. This setup, particularly the temperature control, was described in detail in Ref. [1]. In brief, it consists of a 14.1 T wide-bore superconducting magnet, a ULT MAS probe with a helium gas recirculation system for helium-gas cooling and spinning of the sample down to temperatures of 30 K, and a gyrotron using second harmonic generation to produce mm-wave entering the ULT MAS probe from the top via a waveguide. The HX double resonance probe used is similar in nature to the HC double resonance probe used in Ref. [1], except it has additional replaceable capacitors to switch nuclei for X channel tuning. When no additional capacitors are used on the X channel, the frequency is tuned to ^{13}C, which is the configuration that was used in this work. The system is equipped with a top-loading system for sample exchange that was not present in Ref. [1].

b. Gyrotron System

The gyrotron system used here was designed and assembled by Bridge12. It comprises several key components, including a magnetron-injection gun, an internal cavity, an internal mode converter, an output window, and a collector. Prior to the operation, the gyrotron tube underwent high-temperature maintenance over several days to reduce gas pressure and enhance operational stability.

The magnetron-injection gun (MIG) is designed to generate an electron beam at a nominal cathode voltage ranging from 21 to 23 kV, with a beam current of up to 160 mA. The output electron beam is directed into the internal cavity, which as described in the main text, is configured to support second harmonic generation (SHG) in the transverse electric (TE) mode at 395 GHz at a magnetic field of 7.3 T provided by a Cryomagnetic Inc. cryogen-free superconducting magnet. The internal cavity is thermally isolated from the cavity containing the MIG and internal mode converter, allowing frequency tuning via temperature modulation at approximately 5 MHz/°C, with a Polyscience chiller used to adjust the gyrotron cavity temperature between 10 °C and 70 °C.

The internal mode converter transforms the TE mode produced in the cavity into a Gaussian beam which then exits the gyrotron tube through an output window perpendicular to the tube. The output window consists of a single disk of Al_2O_3. The collector, located at the top of the gyrotron tube, dissipates the spent electron beam and is cooled by an SMC thermos water-cooled chiller, set to 15°C, to maintain stability and prevent overheating during operation. Vacuum maintenance of gyrotron tube is facilitated by an VacIon pump from Duniway Stockroom Corp.

The 7.3T cryogen-free magnet, custom-designed and built by Cryomagnetic Inc., utilizes twisted multiple filamentary NbTi wire and operates at 4.2 K. Cooling of the cryogen-free magnet which is achieved through the combined use of a Sumitomo F-70 water-cooled compressor and an RDK-408D2 Sumitomo cold head. The magnet is energized using a Cryomagnetic Model 4G-100 Superconducting Magnet Power Supply, and its temperature is monitored by a Cryomagnetic TM-612 cryogenic temperature monitor with four measurement channels. The configuration of the cryogen-free magnet allows for a reduced path length from the internal cavity to the output window, enhancing system efficiency. The cavity region is positioned inside the 7.3 T magnet, while the electron gun is located within a separate, independently adjustable gun coil, allowing for optimization during gyrotron testing.

The control system, designed to monitor and control various parameters for the operation of the 395 GHz gyrotron, interfaces a Python-based software developed by Bridge12. The software controls operating parameters, including the electron beam voltage and current, body current, gun coil voltage and current, chiller temperatures, and vacuum levels within the gyrotron tube. The interface features a proportional-integral-derivative (PID) controller, which stabilizes the electron beam current by adjusting the filament current. The control system is powered by a modified 4 kW Spellman X-ray power supply (DF series), which provides the necessary high voltage for system operation. Additionally, the two thermos chiller units—one dedicated to the cavity and the other to the collector—can be controlled remotely, allowing for precise management of the system's thermal environment.

The activation of the gyrotron tube follows a specific sequence, beginning with the initiation of the filament current, followed by the gun coil current, and finally the cathode voltage. The output power and frequency of the mm-wave radiation depend on several factors, including the cathode voltage, beam current, cavity temperature, and magnetic field strength. These parameters were carefully optimized to ensure stable and consistent mm-wave output. During experimental measurements, the cathode voltage was set to 23.6 kV, with the beam current maintained at 150 mA by adjusting the filament current to approximately 2 A through PID control. The mm-wave frequency is tuned by adjusting the cavity temperature, with adjustments ranging from 10°C to 67.5°C. Furthermore, the frequency can be tuned to higher values by reducing the cathode voltage to 21.5 kV, as demonstrated in the main text Figure 2.

c. Room requirements

The chiller water is provided by a custom-built Haskris Chiller, capable of delivering a flow rate of 64 liters per minute to supply water for the four Sumitomo compressors and one SMC chiller. The ULT system requires a power supply of 50 A at 208 V. Each of the four compressors requires a 208 V – 50 A output. All instruments are backed up by an uninterrupted power supply (UPS). The Sumitomo compressor, Haskris Chiller and SMC chiller were located in a separated room, which reduce the noise for user.

d. Top-loading System

Recently, a sample exchange capability under low temperatures was added to the probe through a top-loading system, allowing for more efficient cooling and reduced waiting time for sample exchange. The top-loading system includes a control system, a sample catcher, a vacuum buffer tank, a diaphragm dry vacuum pump, a rotary valve actuator switch, a transfer line, and an adaptor at the top of the probe outer jacket. The interconnection of each component in the top-loading system is illustrated in the accompanying diagram and described in Figure S1.

The outer jacket of the DNP ULT probe is connected to the sample catcher via the transfer line which contains a rotary valve actuator. The control system includes a vacuum gauge to monitor the pressure of the buffer tank, which is vacuumed by the diaphragm dry vacuum pump. Another vacuum/pressure gauge monitors the pressure from the sample catcher to the probe. The top-loading system facilitates successful loading of rotors into the probe at 35 K and ejection of rotors out of the probe at 90 K.

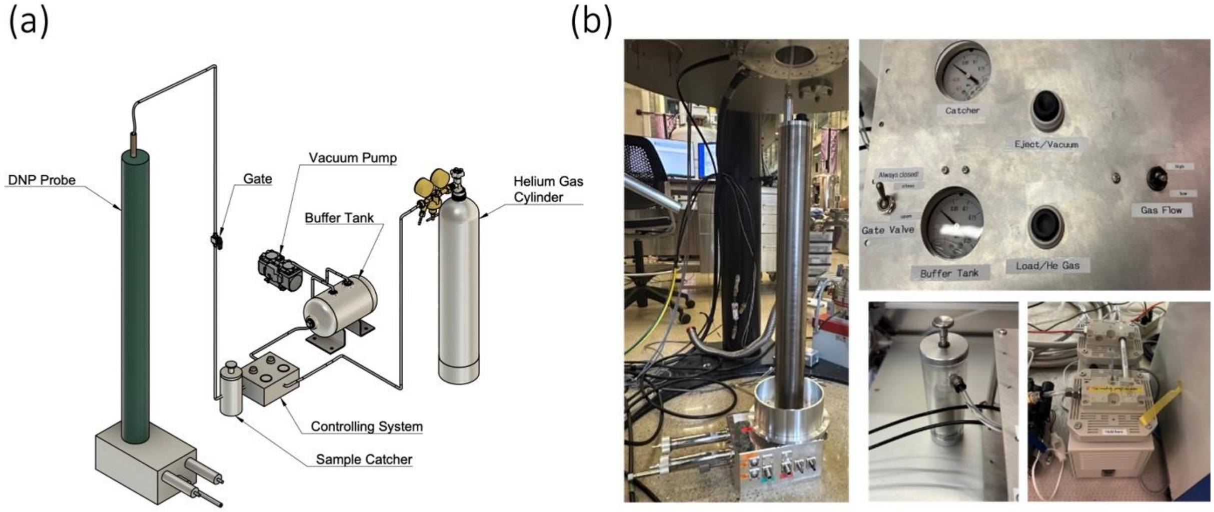

Figure S1: (a) The scheme of top-loading system and (b) the photos of DNP probe with outer jacket, top-loading controlling system, sample catcher and diaphragm vacuum pump.

To insert a new rotor, the DNP probe is first cooled down to 35 K. Then, the rotor is placed into the sample catcher. The sample catcher and the transfer line before the gate are purged with the vacuum pump and refilled with He gas 15 times. After purging, the gate is opened, and the rotor is inserted into the probe by filling it with He gas. After insertion, the gate is immediately closed to avoid exposure to air. Similarly, the rotor can be ejected from the probe when the probe is warmed up to 90 K by vacuuming the transfer line when the gate is open. The rotor is caught by the sample catcher.

e. Relation between gyrotron frequency and cavity temperature

To determine the correlation of the gyrotron cavity temperature with the produced mm-wave frequency, the frequency of the mm-wave beam was measured using a frequency measurement system (FMS) by Bridge12. The FMS operates by mixing a local oscillator frequency ν_{LO} and that of the gyrotron mm-wave frequency vmw, such that $\nu_{\mathrm{IF}} = \lfloor \nu_{\mathrm{mw}} \pm n\nu_{\mathrm{LO}} \rfloor$, where *n* is the harmonic and ν_{IF} is the intermediate frequency. Because it does not feature a bandpass filter, the FMS displays both the upper and lower side band, and all other possible leaked frequencies of the gyrotron from lower stages, if they exist. The FMS software can automatically detect and classify the sidebands and provides a unique frequency measurement with an accuracy ±1 MHz. The gyrotron frequency was measured by removing a portion of the waveguide and placing a mirror approximately 1 m away from the gyrotron cavity output, reflecting at a 45^{o} angle, and positioning the frequency measurement system (FMS) 25.4 cm away from the mirror.

The power output of the gyrotron was measured using a Scientech power meter, placed approximately 1 m away from the output window along the waveguide. To determine the actual power, the measured value was adjusted by a calibration factor of 2.75. This calibration factor was obtained by a combination of water and dry calorimeter to account for the measured (absorbed) power compared to the real power (including both absorbed and reflected power). The reflection/absorption of the Scientech calorimeter head (ACS5000S) was measured on a Vector Network analyser to determine the correction factor. While the gyrotron power is constant at approximately 1 W during cavity temperature tuning, it changes significantly during tuning of any other gyrotron parameters including cathode voltage, beam current, and gyrotron magnetic field.

The relation between the mm-wave frequency and the cavity temperature was found to be approximately linear (see Figure S2). However, a closer fit is obtained when using a second order polynomial (see Figures 2b and S2). We also observed that the relation between the mm-wave frequency and the cavity temperature was subject to evolution over time (see Figure S2). In our current setup, the mm-wave frequency is measured by replacing a section of the waveguide with a mirror to divert the mm-wave beam to a frequency measurement device (see the Methods section). To ensure a sufficient resolution of the frequency during the acquisition of DNP profiles, the mm-wave frequency was measured at the beginning and the end of each DNP profile, and at several intermediate points (typically every 5°C or 25 MHz). The quadratic fit of Figure 2b was found to predict the frequency of the resulting dataset with a root mean square error of 2.7 MHz (see Figure S3). While mm-wave frequency fluctuations occur due to sensitivity to slight changes in proportional-integral-derivative (PID)-controlled parameters, such as beam current and cavity temperature, the fluctuations are minor and do not distort the broad DNP features discussed in the later sections. Furthermore, the beam current (and thus indirectly, the output power) was held stable to about 0.3 % by the PID controller in the gyrotron control system. Details on the instrumentation setup for mm-wave frequency and power measurements are provided in the Methods section and SI Section 1e.

The frequency response of the gyrotron to its cavity temperature was measured twice at different dates (on July 18th and September 3rd, 2024), using the measurement device described above. In both cases, the temperature of the cavity was stepped from low to high temperature, letting the cavity stabilize during 10 min before recording the frequency. The two calibration curves yielded slightly different results. Figure S2 shows that a linear regression fits the first calibration data set well with R_2 = 0.9994, with randomly dispersed residuals. The calibration second data set is not fit well by the linear regression (R_2 = 0.998) and the residuals show a clear trend. Adding a quadratic correction makes the fit better R_2 = 0.9997, with a less pronounced trend of the residuals.

Because we found that the relation between temperature and frequency was subject to variation over time, we recorded the DNP profiles monitoring the frequency at multiple points along the acquisition of the profile to be able to correct for possible drifts. During the acquisition of five different DNP profiles, the mm-wave frequency was measured at a total of 57 temperatures. We used this data set and compared it against the prediction of the calibration curves of Figure S2. Figure S3 shows the deviation between the experiment and predicted frequency $\nu_{\mathrm{exp}} - \nu_{\mathrm{cal}}$, for the 57 measurements and the three calibration curves of Figure S2. The root mean square error (RMSE) on the prediction by each calibration (which corresponds to the root mean square of the data points on the plot) is shown on each plot. The RMSE of the prediction using the quadratic calibration curve obtained from the data set of September 3rd is equal to 2.8 MHz, which is about twice smaller than for the two other calibration curves. Furthermore, the deviations for this calibration curve does not show a clear trend as they do for the two other curves. We therefore chose to use the quadratic calibration curve to compute the frequency in the DNP profile shown in this work. The RMSE of 2.8 MHz is the result of the uncertainty on both the gyrotron frequency and the frequency measurement. It therefore sets an upper bound for the standard deviation of the mm-wave frequency produced by the gyrotron.

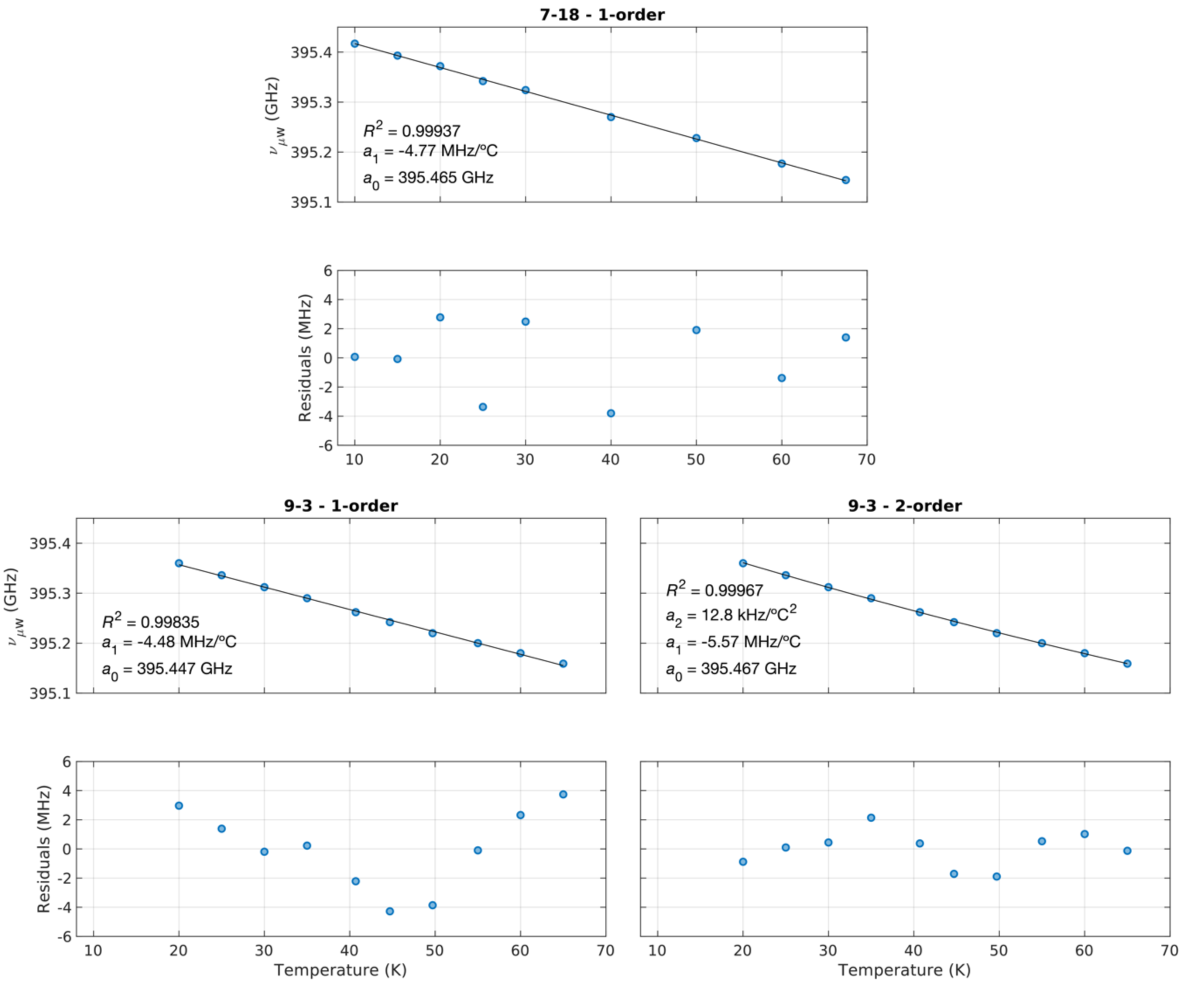

Figure S2: Linear regression of the frequency vs. temperature data set acquired on July 18th, and linear and quadratic regression of the data set acquired on September 3rd. The values a_0, a_1, and a_2 on the plots are the polynomial coefficients of the fits where the index indicates the order of the term associated with it.

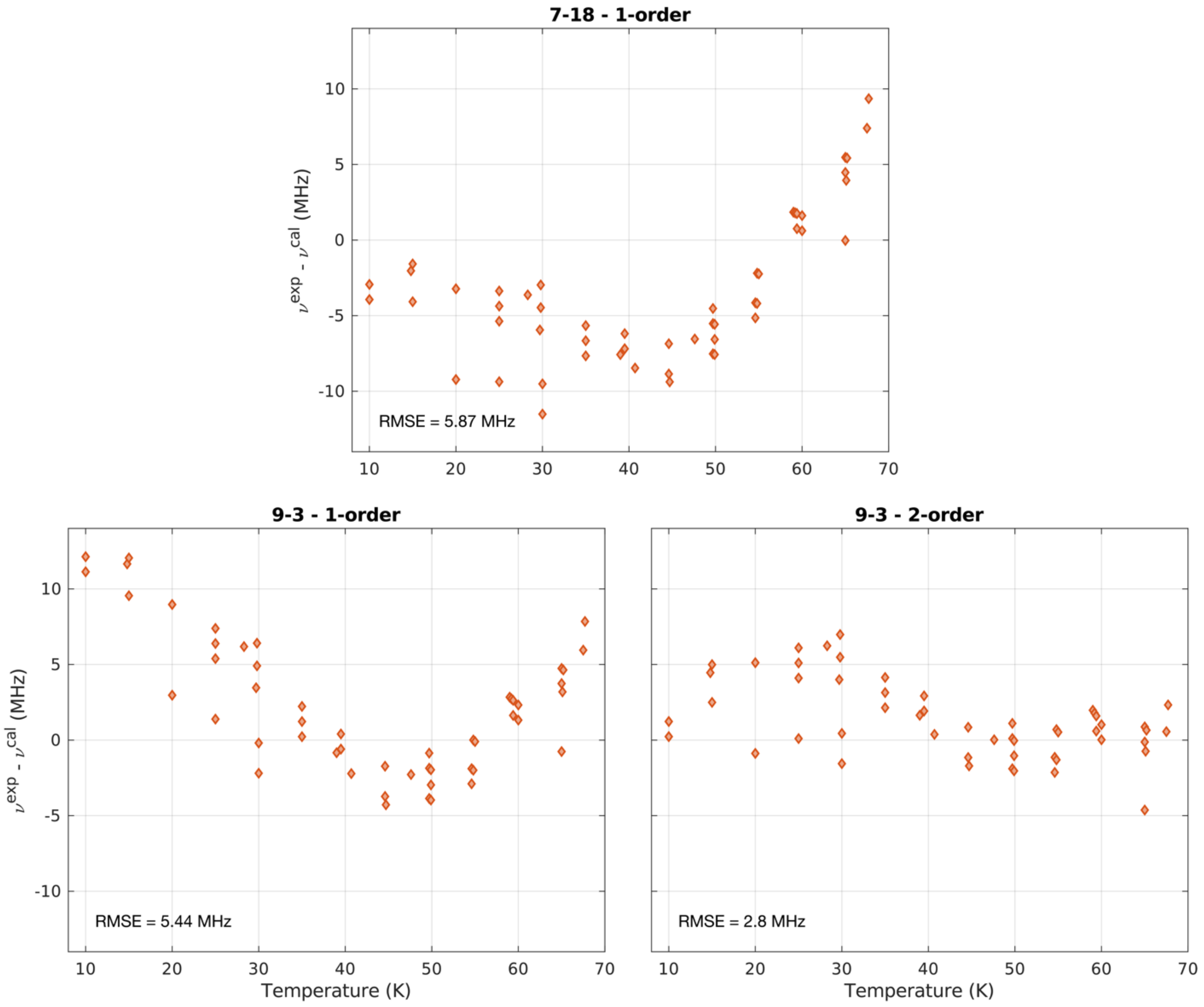

Figure S3: Difference between the measured mm-wave frequency ν_{exp} and the frequency calculated ν_{cal} using the three calibration curves of Figure S2. The measured mm-wave frequencies correspond to a data set of 57 temperature – frequency pairs obtained during the course of five individual DNP profiles.

2. Experimental

a. NMR measurements

^{13}C NMR spectra were acquired using the Delta v6.0 NMR acquisition and data processing software from JEOL. Saturation recovery measurements were performed with the pulse sequence: (t_{sat}) – τ – $\pi/2$-detection, where the saturation pulse train uses $t_{sat} = (\pi/2 – t_{wait})n = 10$ ms, with $t_{wait} = 1$ ms, $\tau = 60$ s and $\pi/2 = 4.5$ µs or 7.0 µs with 15 dB or 24 dB attenuation at RT and ULT, respectively, from the full power for both saturation and detection. For DNP experiments, continuous wave (CW) mm-wave irradiation was applied throughout the pulse sequence, and the data was acquired with two scans at each mm-wave frequency. For T_1 and T_{DNP} build-up curve measurements, the same saturation-recovery pulse sequence was used without and with mm-wave irradiation respectively, and by varying the time interval τ from 0.1 s to 6 h. The spectra were exported as raw FID data from the Delta software and processed using the Python DNPLab package v2.1.19.

b. EPR measurements

EPR experiments were performed on a home-built 13.8 T dual DNP/EPR spectrometer equipped with a closed-cycle helium cooling system and using a home-built pulse forming unit, an amplifier multiplier chain (AMC), and a quasi-optical induction mode bridge, as described elsewhere.[2,3] Frequency-swept EPR signals were measured using an echo sequence $(t_p)_{\varphi 1} - \tau_e - (t_p)_{\varphi 2} - \tau_e - (\text{detection})_{\varphi d}$ with a 16-step phase cycling $\varphi_1 = [0°_4, 90°_4, 180°_4, 270°_4]$ and $\varphi_2 = [0°, 90°, 180°, 270°]_4$ for the two pulses and $\varphi_d = \varphi_1 - 2\varphi_2$ for detection. At RT, the pulse length and echo time were t_p = 1.6 µs and τ_e = 0.5 µs, respectively, and the signal was averaged over 100 shots with a repetition time of 2 ms. At 35 K, the pulse length and echo time were t_p = 1.8 µs and τ_e = 0.85 µs, respectively and the signal was recorded with a single shot and a repetition time of 1 s. Saturation experiments were performed by adding a pump pulse of length t_{pump} = 10 ms at the same frequency as the probe, with a delay τ_d of 1 µs between the pump and probe blocks. The pulse length and echo time τ_e for each temperature were the same as in the frequency-swept EPR experiments with 50 averages at RT and a single shot at 35 K and a repetition time of 14 ms and 0.5 s for the RT and 35 K experiments respectively.

The spin counting was performed on a CW X-band Bruker Elexsys E500 spectrometer.

c. Saturation Recovery T_1 and T_{DNP} measurements

Saturation recovery measurements were acquired for the microdiamond sample presented in the main text, using the pulse sequence and parameters described in the Methods sections, for both mm-wave-on and -off conditions. T_1 and T_{DNP} measurements were processed using the DNPLab Python package of data taken from the JEOL Delta software. The FIDs were left-shifted to remove the initial filter signal and Fourier transformed using zero-filling to 1226 points. The single ^{13}C NMR signal of diamond was then integrated by summing the spectrum intensity on a window of 23 ppm. The signal integrals along time *t* were fitted with a stretched exponential model

$$M(t) = M_\infty - (M_\infty - M_0)\exp\left(-\left(\frac{t}{T}\right)^{\beta}\right), \qquad \text{Eq. S1}$$

where *T* and *β* are build-up time constant (T_1 and T_{DNP}, for mm-wave-off and -on measurements, respectively) and the stretch factor between 0 and 1, respectively. The average build-up time constant was obtained as

$$T^{\text{av}} = \frac{T}{\beta}\Gamma\left(\frac{1}{\beta}\right), \qquad \text{Eq. S2}$$

where Γ is the gamma function.

RT saturation recovery experiments were acquired using 6 kHz MAS both without (Fig. S4a) and with mm-wave irradiation at 395.2015 GHz (positive enhancement peak, Fig. S4b) and 395.366 GHz (negative enhancement peak, Fig. S4c) to obtain the T_{DNP} and T_1 constants, respectively. These curves were subsequently fitted using Eq. S1, giving mean values of T_1^{av} = 780 s, $T_{\text{DNP}}^{\text{av}}$ (395.2015 GHz) = 608 s, and $T_{\text{DNP}}^{\text{av}}$ (395.366 GHz) = 468 s, with the fit parameters detailed in Table S1. Because $T_{\text{DNP}}^{\text{av}} < T_1^{\text{av}}$ the on/off enhancements $\epsilon_{\text{on/off}}$ of the DNP profiles in Figure 3 only coincide with the absolute enhancements for very long delay times τ between saturation and acquisition, on the order of ~10^3 s. Using the saturation recovery experiments of the mm-wave-on and -off experiments, we computed the absolute and on/off enhancements (see Eqs. 1 and 2) at both delay t = 60 s and as *t* approaches infinity.

T_1 saturation recovery measurements were also performed at RT under static conditions (Fig. S4d) and at 100 K (Fig. S4e) and 35 K (Fig. S4f) under MAS conditions. Under static RT conditions T_1 was fit with and $T_1^{av} = 136$ s, and at 100 K and 35 K with 5 kHz MAS the T_1 was fit with and T_1^{av} = 5553 s and 5207 s, respectively. We note that the fits at 100 and 35 K only give an order-of-magnitude estimate due strong noise of the saturation recovery at these temperatures, which is probably due to instabilities in the MAS rate at ULT introducing T_1 noise over the course of the hours-long experiment

Table S1. Saturation recovery curve fittings using a stretched exponential fit (see Eq. S1), where the average time constant is calculated using the gamma function distribution (see Eq. S2). mm-wave-on measurements indicated by (+) and (-) correspond to irradiation at 395.2015 and 395.355 GHz, respectively. The measured values at ULT are only rough estimates so they are given in parenthesis.

Temperature (K)	MAS frequency (kHz)	mm-wave irradiation	Stretched exponential fit		
			$T_{1/DNP}^{av}$ (s)	$T_{1/DNP}$ (s)	Stretch factor β
298	0	off	136	96.2	0.63
298	6	off	780	463	0.55
100	5	off	(5553)	(2610)	(0.48)
35	5	off	(5207)	(816)	(0.33)
298	6	on (+)	608	445	0.65
298	6	on (-)	468	337	0.64

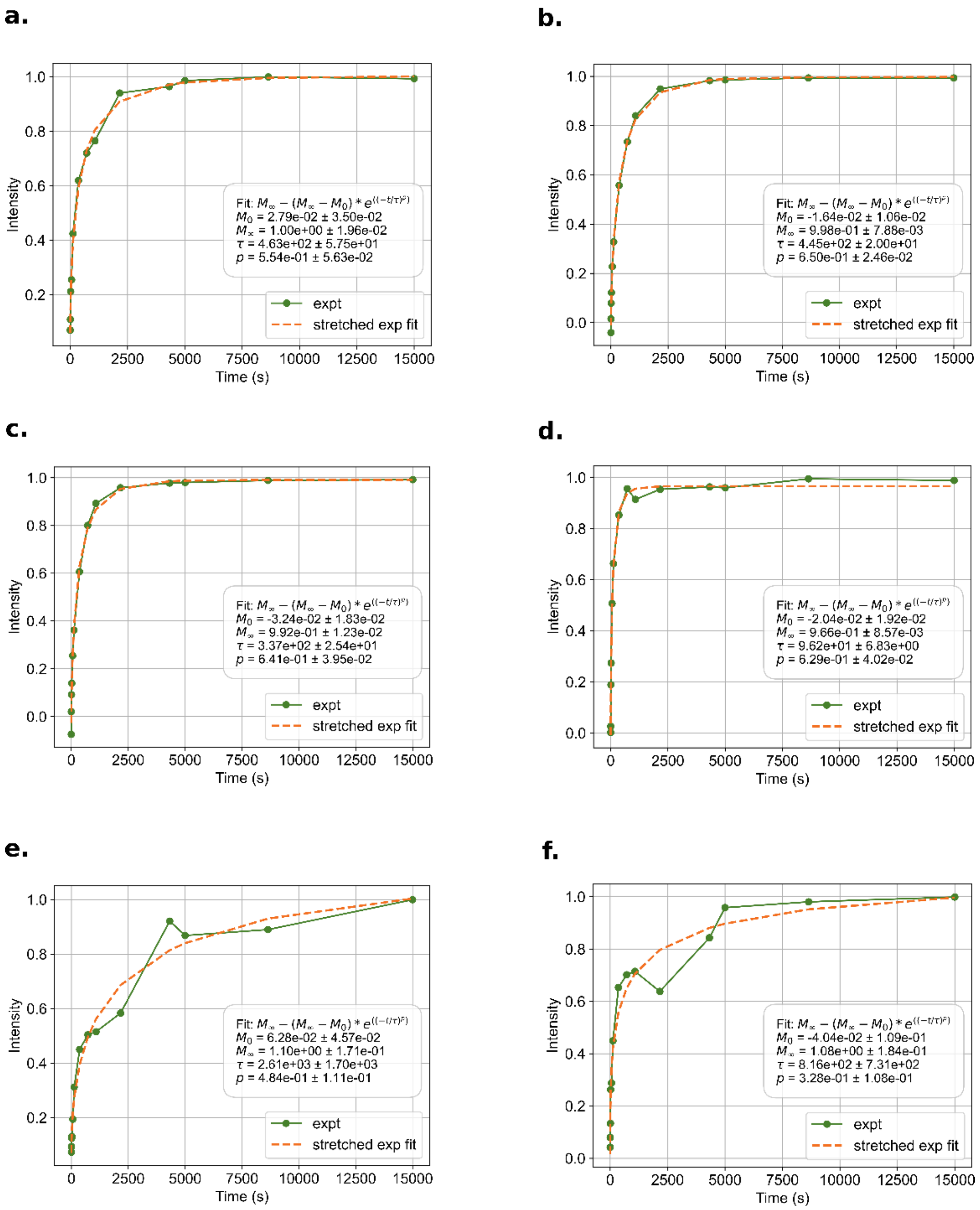

Figure S4: Saturation recovery experiments taken at various conditions. **a**-**d**. are each taken at RT, with (a) at mm-wave-off MAS condition, **b**. at mm-wave-on at the positive DNP enhancement peak (395.2015 GHz), **c.** at mm-wave-on on at the negative DNP enhancement peak (395.366 GHz), and (d) at mm-wave-off Static Condition. **e**. is taken at 100 K at mm-wave-off MAS condition while **f.** is taken at 35 K at mm-wave-off MAS condition. All are fitted using the stretched exponential function with fit parameters and equation shown on each plot.

d. DNP profiles at room temperature on other HPHT diamonds samples

DNP profiles were acquired for three HPHT diamond samples manufactured by Hyperion with different P1 concentrations (10-20, 100, and 100's of ppm) and a size of 100 µm, using the same experimental procedure as for those in the main text of the paper. The normalized DNP profiles are shown in Figure S5. The DNP profiles in absolute value are shown in the inset.

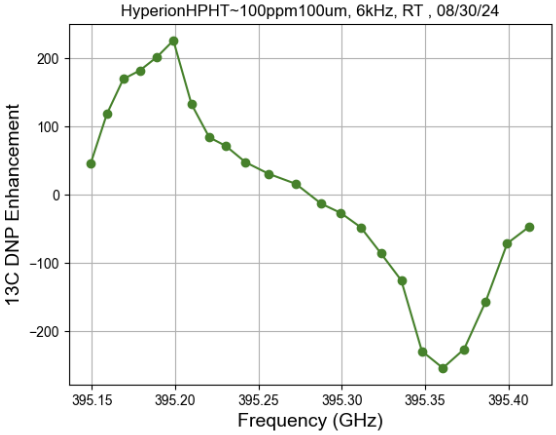

Figure S5: DNP profile for HPHT diamonds by Hyperion.

3. Theory

a. Electron polarization

The electron polarization at thermal equilibrium is calculated using Boltzmann's law

$$P_0 = \tanh\left(\frac{\hbar|\omega_0|}{2K_\mathrm{B}T}\right) = \tanh\left(\frac{\mu_\mathrm{B}B_0|g|}{2K_\mathrm{B}T}\right), \qquad \text{Eq. S3}$$

where $\hbar$, ω_0, K_B, T, μ_B, B_0, and g are the reduced Planck constant, the Larmor frequency of the electron, Boltzmann's constant, the lattice temperature, Bohr's magneton, the static magnetic field strength, and the g-factor of the electron, respectively. The polarization varies along the EPR spectrum, but a single value can be approximated using the isotropic g-factor.

b. Hole burning models

This section presents the two approaches that were used in this work to simulate hole burning, i.e., the behavior of the EPR line under saturation by mm-wave irradiation: Vega's electron spectral diffusion model (eSD)[4,5] and an analytical solution to the diffusion equation, based on recent work by Wenckebach.[6] In both cases, three mechanisms influence electron spin polarization: mw-wave irradiation, $T_{1\mathrm{e}}$ relaxation, and spectral diffusion. Only electron Zeeman order is explicitly accounted for (electron spin dipolar order is neglected). The influence of ^{13}C nuclear spins on the electron spin dynamics is neglected. These models were developed in the context of static DNP and do not account for MAS. They should therefore be seen as phenomenological.

Vega's eSD model: In Vega's model, the EPR line is divided into N bins with frequencies ω_k and intensities f_k for which the electron spin polarization $P(\omega_\mathrm{k})$ is assumed to be homogeneous. The intensity of the line is normalized so that $\sum_{k=1}^{N} f_k = 1$. This model was presented in several publications. The form described here is closest to that presented in Ref. [4,5]. However, we have found some small mistakes and typos in the publications (eg: missing $\hbar$ in a Boltzmann factor and signs) that we attempted to correct in this work.

The shape of the EPR line under saturation by mm-wave irradiation at the steady-state is obtained by solving numerically the differential equation

$$\frac{d}{dt}\vec{P}(t) = (\boldsymbol{W}_\mathrm{mw} + \boldsymbol{R}_1 + \boldsymbol{R}_\mathrm{D})\vec{P}(t), \qquad \text{Eq. S4}$$

where $\vec{P}(t) = [1, P_1, P_2, \ldots, P_N]^{\mathrm{T}}$ is a vector representing the polarizations in the *N* bins. The first unity term in the vector allows to compute relaxation while keeping the differential equation homogeneous. The three matrices $\boldsymbol{W}_{\mathrm{mw}}$, $\boldsymbol{R}_1$, and $\boldsymbol{R}_{\mathrm{D}}$ acting on the polarization vector represent mm-wave irradiation, $T_{1\mathrm{e}}$ relaxation, and spectral diffusion, respectively. We did not include the DQ and ZQ SE transitions assuming that they are weak in our experimental conditions. $\boldsymbol{W}_{\mathrm{mw}}$ represents the saturation of the single quantum transitions and only contains non-zero elements on the diagonal, which can be represented as

$$(\boldsymbol{W}_{\mathrm{mw}})_{kk} = -\frac{\omega_1^2 T_2}{1+(\omega_k-\omega_{\mathrm{mw}})^2 T_2^2}, \qquad \text{Eq. S5}$$

where ω_1, T_2, ω_k, and ω_{mw} are the strength of the mm-wave field in rad.s^{-1}, the electron spin-spin relaxation time constant, the electron spin resonance frequency of bin *k*, and the mm-wave frequency, respectively. The action of $\boldsymbol{R}_1$ can be represented in the subspace of electron spin *k* as

$$\frac{d}{dt}\begin{pmatrix} 1 \\ P_k(t) \end{pmatrix} = \begin{pmatrix} 0 & 0 \\ \frac{P_{0,k}}{T_1} & -\frac{1}{T_1} \end{pmatrix}\begin{pmatrix} 1 \\ P_k(t) \end{pmatrix}, \qquad \text{Eq. S6}$$

where $T_{1,k} = T_{1\mathrm{e}}$ is assumed to be constant across the EPR line and $P_{0,k}$ is the Boltzmann polarization for bin *k*, calculated by setting $\omega_0 = \omega_k$ in Eq. S3. The non-zero matrix elements of $\boldsymbol{R}_1$ can therefore be written as

$$(\boldsymbol{R}_1)_{k1} = \frac{P_{0,k}}{T_1}, \qquad \text{Eq. S7}$$

$$(\boldsymbol{R}_1)_{kk} = -\frac{1}{T_1}.$$

Finally, $\boldsymbol{R}_{\mathrm{D}}$, which represents spectral diffusion, is the only matrix with non-diagonal terms, which connects bins with each other. It can be represented as the sum

$$\boldsymbol{R}_{\mathrm{D}} = \sum_{j>k} \boldsymbol{R}_{\mathrm{D},kj}, \qquad \text{Eq. S8}$$

of matrices in the subspace of electron spin *k* and *j*,

$$\boldsymbol{R}_{\mathrm{D},kj} = \frac{\Lambda^{\mathrm{eSD}}}{(\omega_k-\omega_j)^2}\frac{1}{1+\eta_{kj}}\begin{pmatrix} -\eta_{kj} f_j & +f_j \\ +\eta_{kj} f_k & -f_k \end{pmatrix}, \qquad \text{Eq. S9}$$

where Λ^{eSD}, f_k and f_j are a coefficient describing the efficiency of spectral diffusion in s^{-3} and the normalized EPR intensities of bins *k* and *j*, respectively. The thermal correction factor

$$\eta_{kj} = \frac{P_{0,j}}{P_{0,k}}, \qquad \text{Eq. S10}$$

ensures that spectral diffusion preserves the gradient of polarization at Boltzmann equilibrium that arises from the difference in Larmor frequency of the individual spin packets. Note that the thermal correction factor in Eq. S10 is defined in this way in Ref. [4]. An alternative form of this term is given in several other references by the same group (eg, Ref. [5,7,8]), which is based on Boltzmann factors

$$\eta_{kj} = \exp\left(-\frac{\hbar}{K_{\mathrm{B}T}}(\omega_k - \omega_j)\right). \qquad \text{Eq. S11}$$

According to Eq. 16b in Ref. [7] and Eq. 69 in Ref. [8], the expression in Eq S11 is supposed to be equal to that in Eq. S10. However, these equations are in fact not equal; the proposed Boltzmann factor gives a population ratio, and not a polarization ratio as in Eq. S10. We performed test simulation of the eSD model switching off mm-wave saturation (that is, setting $\omega_1 = 0$). In this case, only spectral diffusion is active. If the thermal correction factor is correct, the polarization across the EPR line, should remain constant at all times. We found that Eq. S10 did produce the appropriate gradient of polarization (as predicted by Eq. S3), while not Eq. S11 (see Figure S6). We therefore chose to use Eq. S10.

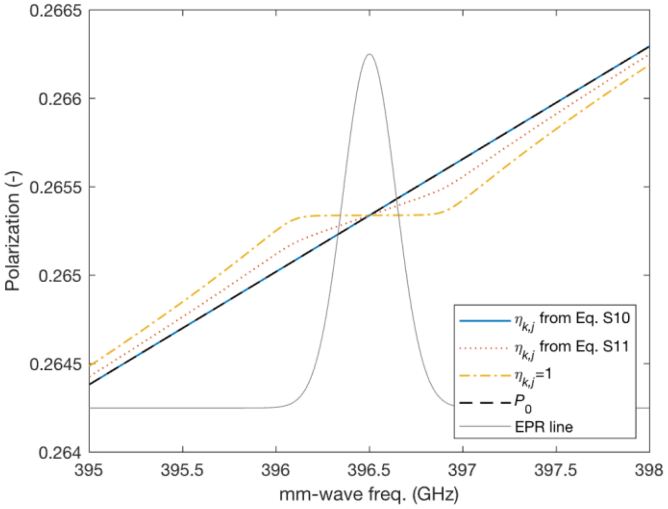

Figure S6: Verification of the validity of the thermal correction factor given in Eq. S10. The polarization as a function of frequency is simulated using the eSD (see Eq. S4) for a Gaussian EPR line with standard deviation of 100 MHz centered at 396.5 GHz (represented by a grey line in arbitrary units), with no mm-wave irradiation ($\omega_1 = 0$), $T_2 = 1$ µs (which does not influence the simulation because $\omega_1 = 0$), $T_1 = 1$ ms, and $\Lambda^{\mathrm{eSD}} = 4000\ \mu\mathrm{s}^{-3}$. The black dashed line represents the initial polarization, computed using Eq. S3. The blue, red dotted, and yellow dashed dotted lines represent the final polarization (at $t_{\max} = 5 \cdot T_{1e} = 5$ ms) if the thermal correction factor is computed using Eq. S10, using Eq. S11, or set to 1, respectively.

In all cases, we used the differential equation solver of MATLAB *ode15s*, which is optimized for problems with timescales ranging on different orders of magnitude. The differential equation was solved on a time range from 0 to $t_{\max} = 5 \cdot T_{1e}$. The last vector $\vec{P}(t_{\max})$ computed by *ode15s* was assumed to represent the electron spin polarization at dynamic equilibrium.

Analytical solution to the spectral diffusion equation: An alternative to Vega's eSD is to treat spectral diffusion as a standard 1-dimensional diffusion equation. A difficulty that arises in this case is how to obtain the frequency dependence of the diffusion coefficient. Wenckebach recently proposed an approach based on Monte Carlo simulation.[6] Here, we use a simple approximation of the diffusion equation where the diffusion coefficient is assumed to be constant across the EPR line, as proposed by Vaneeckhaute *et al*.[9] This approach has the advantage of yielding an analytical solution with a limited number of free parameters. Under the assumption of constant T_{1e} and diffusion coefficient D across the EPR line, the diffusion equation can be expressed as

$$\frac{\partial}{\partial t}P(\nu) = -\pi\omega_1^2\, h\big(\omega - \omega_{\mu\mathrm{w}}\big)P(\omega) + D\frac{\partial^2}{\partial\omega^2}P(\omega) + \frac{P_0 - P(\omega)}{T_{1e}}, \qquad \text{Eq. S12}$$

where *h* and *D* are the homogeneous broadening and the spectral diffusion coefficient, respectively. If we further assume that the homogeneous broadening is small compared to the inhomogeneous broadening, the mm-waves are only on resonance with spins of the exact same frequency. Eq. S12 then becomes

$$\frac{\partial}{\partial t} P(\omega) = -\pi\omega_1^2\, P(\omega)\delta(\omega - \omega_{\mathrm{mw}}) + D\frac{\partial^2}{\partial\omega^2} P(\omega) + \frac{P_0 - P(\omega)}{T_{1\mathrm{e}}}. \qquad \text{Eq. S13}$$

At equilibrium, that is, when Eq. S13 is null, the diffusion equation has the solution

$$P_{\mathrm{mw}}(\omega) = P_0\left(1 - \exp\left(-\frac{|\omega - \omega_{\mathrm{mw}}|}{\Lambda}\right)\right), \qquad \text{Eq. S14}$$

where $\Lambda = (DT_{1\mathrm{e}})^{1/2}$ is the spectral diffusion length.

c. DNP model using analytical equations

This section shows the derivation of simple formula for the profiles of the solid effect (SE), the cross effect (CE), and the truncated cross effect (tCE) for the case where spectral diffusion can be neglected. This derivation also requires the hypothesis that the electron spin-lattice relaxation time $T_{1\mathrm{e}}$ is constant across the EPR line, leading to a constant saturation efficiency across the line. Alternatively, assuming full saturation yields the same result. It is further assumed that nuclear spin diffusion averages nuclear polarization across the sample.

Solid effect case: If there is no electron spectral diffusion, the polarization of electron spins on resonance with double- and zero-quantum transitions (DQ and ZQ) are not affected by each other nor they are affected by depolarization of electron spin on resonance with single quantum transition (SQ). In this case, SE affects the nuclear polarization only for nuclear spins interacting with electrons on resonance with the ZQ and DQ transitions, yielding

$$P_{\mathrm{I}}^{\mathrm{SE,ZQ}}(\omega_{\mathrm{mw}} + \omega_{\mathrm{I}}) = -\chi P_0, \qquad \text{Eq. S15}$$

and

$$P_{\mathrm{I}}^{\mathrm{SE,DQ}}(\omega_{\mathrm{mw}} - \omega_{\mathrm{I}}) = +\chi P_0, \qquad \text{Eq. S16}$$

where ω_{I}, χ, and P_0 are the absolute value of the nuclear Larmor frequency, a factor describing the dynamic efficiency of the saturation of the SE transitions, and the electron polarization at Boltzmann equilibrium (see Eq. S3), respectively. Assuming that nuclear spin diffusion equalizes polarization across the sample and that the nuclear Boltzmann polarization and nuclear relaxation are negligible, the bulk nuclear polarization is the weighed summed of the two contributions of Eqs. S15 and S16

$$\begin{aligned} P_{\mathrm{I}}^{\mathrm{SE}}(\omega_{\mathrm{mw}}) &= f(\omega_{\mathrm{mw}} + \omega_{\mathrm{I}})P_{\mathrm{I}}^{\mathrm{SE,ZQ}} + f(\omega_{\mathrm{mw}} - \omega_{\mathrm{I}})P_{\mathrm{I}}^{\mathrm{SE,DQ}} \\ &= \chi P_0\big(f(\omega_{\mathrm{mw}} - \omega_{\mathrm{I}}) - f(\omega_{\mathrm{mw}} + \omega_{\mathrm{I}})\big), \end{aligned} \qquad \text{Eq. S17}$$

The shape of the SE profile is then given by Eq. S17, dropping constant factors

$$f_{\mathrm{SE}}(\omega_{\mathrm{mw}}) = f(\omega_{\mathrm{mw}} - \omega_{\mathrm{I}}) - f(\omega_{\mathrm{mw}} + \omega_{\mathrm{I}}), \qquad \text{Eq. S18}$$

which can be obtained concisely as the convolution integral

$$f_{\mathrm{SE}}(\omega_{\mathrm{mw}}) = (f * u)[\omega_{\mathrm{mw}}], \qquad \text{Eq. S19}$$

of the EPR line with the function

$$u(\nu) = \delta(\omega - \omega_I) - \delta(\omega + \omega_I), \qquad \text{Eq. S20}$$

where δ is the Dirac delta function.

Cross effect case: The CE transfers the polarization difference between two electrons to a nuclear spin via triple spin flips, provided the Larmor frequency difference of the two electrons $\omega_1 - \omega_2$ matches the nuclear Larmor frequency ω_I. At equilibrium, a nuclear spin interacting with such a pair of electron spins has polarization[10,11]

$$P_\mathrm{I} = \frac{P_1 - P_2}{1 - P_1 P_2}, \qquad \text{Eq. S21}$$

where P_1 and P_2 are the polarizations of the two electron spins. The denominator is a normalization constant that only plays a role at high electron polarization. Assuming that spin diffusion averages the nuclear spin polarization, the bulk nuclear polarization is given by the weighted average over all possible electron spin pairs fulfilling the CE matching condition

$$P_\mathrm{I} = \frac{1}{F_\mathrm{N}} \int d\omega f(\omega) f(\omega - \omega_\mathrm{I}) \frac{P(\omega) - P(\omega - \omega_\mathrm{I})}{1 - P(\omega) P(\omega - \omega_\mathrm{I})}, \qquad \text{Eq. S22}$$

where $P(\omega)$ is the electron polarization at frequency ω in the EPR line, and the normalization factor condition

$$F_\mathrm{N} = \int d\omega f(\omega) f(\omega - \omega_\mathrm{I}). \qquad \text{Eq. S23}$$

The term $f(\omega_\mathrm{I})f(\omega - \omega_\mathrm{I})/F_\mathrm{N}$ in Eq. S22 expresses the probability for a particular pair of electron spins to fulfill the CE matching condition, given the EPR intensities $f(\omega_\mathrm{I})$ and $f(\omega - \omega_\mathrm{I})$. In absence of mm-wave irradiation, the $P(\omega_\mathrm{I}) - P(\omega - \omega_\mathrm{I})$ is equal to the nuclear Boltzmann polarization $P_{\mathrm{I}0}$ and Eq. S22 predicts $P_\mathrm{I} = P_{\mathrm{I}0}$. In this case, CE serves as a T_1 relaxation mechanism for nuclear spins. CE DNP consist of creating an out-of-equilibrium difference between electron spins via mm-wave (or microwave) irradiation that then transfers spontaneously to nuclear spins.

If there is no spectral diffusion, triple spin flips only result in hyperpolarization between the electron spins being saturated (with $\omega = \omega_\mathrm{mw}$) and those satisfying $\omega = \omega_\mathrm{mw} - \omega_\mathrm{I}$ and $\omega = \omega_\mathrm{mw} + \omega_\mathrm{I}$, on the left and on the right of the irradiation frequency, respectively. In these two cases, Eq. S21 gives the polarization of nuclear spins interacting with such electron spin pairs are

$$P_\mathrm{I}^\text{CE,left}(\omega_\mathrm{mw}) = \frac{P(\omega_\mathrm{mw}) - P(\omega_\mathrm{mw} - \omega_\mathrm{I})}{1 - P(\omega_\mathrm{mw}) P(\omega_\mathrm{mw} - \omega_\mathrm{I})}, \qquad \text{Eq. S24}$$

and

$$P_\mathrm{I}^\text{CE,right}(\omega_\mathrm{mw}) = \frac{P(\omega_\mathrm{mw} + \omega_\mathrm{I}) - P(\omega_\mathrm{mw})}{1 - P(\omega_\mathrm{mw}) P(\omega_\mathrm{mw} + \omega_\mathrm{I})}. \qquad \text{Eq. S25}$$

Because there is no spectral diffusion, the polarization of the left and right partners is that of thermal equilibrium P_0

$$P(\omega_\mathrm{mw} - \omega_I) = P(\omega_\mathrm{mw} + \omega_\mathrm{I}) = P_0, \qquad \text{Eq. S26}$$

and assuming a homogeneous T_{1e} across the EPR line (or that saturation is infinite), the saturation factor is constant across the EPR line, yielding

$$P(\omega_{\mathrm{mw}}) = P^{\mathrm{sat}}. \qquad \text{Eq. S27}$$

We therefore have

$$P_{\mathrm{I}}^{\mathrm{CE,left}}(\omega_{\mathrm{mw}}) = \frac{P^{\mathrm{sat}} - P_0}{1 - P^{\mathrm{sat}} P_0}. \qquad \text{Eq. S28}$$

and

$$P_{\mathrm{I}}^{\mathrm{CE,right}}(\omega_{\mathrm{mw}}) = \frac{P_0 - P^{\mathrm{sat}}}{1 - P_0 P^{\mathrm{sat}}}, \qquad \text{Eq. S29}$$

Hence, the integral of Eq. S22 is the sum of the two terms of Eqs. S28 and S29, with the weights, $f(\omega_{\mathrm{mw}})f(\omega_{\mathrm{mw}} - \omega_{\mathrm{I}})/F_{\mathrm{N}}$ and $f(\omega_{\mathrm{mw}})f(\omega_{\mathrm{mw}} + \omega_{\mathrm{I}})/F_{\mathrm{N}}$, respectively, yielding

$$\begin{aligned} P_{\mathrm{I}}^{\mathrm{CE}}(\omega_{\mathrm{mw}}) &= \frac{f(\omega_{\mathrm{mw}})f(\omega_{\mathrm{mw}} - \omega_{\mathrm{I}})}{F_{\mathrm{N}}} P_{\mathrm{I}}^{\mathrm{CE,left}}(\omega_{\mathrm{mw}}) + \frac{f(\omega_{\mathrm{mw}})f(\omega_{\mathrm{mw}} + \omega_{\mathrm{I}})}{F_{\mathrm{N}}} P_{\mathrm{I}}^{\mathrm{CE,right}}(\omega_{\mathrm{mw}}) \qquad \text{Eq. S30} \\ &= \frac{1}{F_{\mathrm{N}}} \frac{P_0 - P^{\mathrm{sat}}}{1 - P_0 P^{\mathrm{sat}}} f(\omega_{\mathrm{mw}}) \big(f(\omega_{\mathrm{mw}} + \omega_{\mathrm{I}}) - f(\omega_{\mathrm{mw}} - \omega_{\mathrm{I}}) \big) . \end{aligned}$$

The shape of the CE profile is then given by Eq. S30, dropping the constant factors

$$f_{\mathrm{CE}}(\omega_{\mathrm{mw}}) = f(\omega_{\mathrm{mw}}) \big(f(\omega_{\mathrm{mw}} + \omega_{\mathrm{I}}) - f(\omega_{\mathrm{mw}} - \omega_{\mathrm{I}}) \big) . \qquad \text{Eq. S31}$$

As for the SE, this can be computed in a compact way as a convolution integral (or as the product of the EPR line with the SE profile)

$$f_{\mathrm{CE}}(\omega_{\mathrm{mw}}) = f(\omega_{\mathrm{mw}}) \big((f * u)[\omega_{\mathrm{mw}}] \big) = f(\omega_{\mathrm{mw}}) f_{\mathrm{SE}}(\omega_{\mathrm{mw}}). \qquad \text{Eq. S32}$$

Truncated cross effect case: the tCE without spectral diffusion can be computed in a similar way as the CE. Let us call f_{S} and f_{F} the EPR lineshape of the slow- and fast-relaxing spins, respectively. For the case where spectral diffusion among the slow-relaxing spins can be neglected, triple spin flips leading to nuclear hyperpolarization only occur for the saturated slow-relaxing spin (with $\omega_{\mathrm{S}} = \omega_{\mathrm{mw}}$) and the fast-relaxing spins satisfying $\omega_{\mathrm{F}} = \omega_{\mathrm{mw}} - \omega_{\mathrm{I}}$ and $\omega_{\mathrm{F}} = \omega_{\mathrm{mw}} + \omega_{\mathrm{I}}$. Eqs. S24 and S25 can then be adapted to the tCE as

$$P_{\mathrm{I}}^{\mathrm{tCE,left}}(\omega_{\mathrm{mw}}) = \frac{P_{\mathrm{S}}(\omega_{\mathrm{mw}}) - P_{\mathrm{F}}(\omega_{\mathrm{mw}} - \omega_{\mathrm{I}})}{1 - P_{\mathrm{S}}(\omega_{\mathrm{mw}}) P_{\mathrm{F}}(\omega_{\mathrm{mw}} - \omega_{\mathrm{I}})}, \qquad \text{Eq. S33}$$

and

$$P_{\mathrm{I}}^{\mathrm{tCE,right}}(\omega_{\mathrm{mw}}) = \frac{P_{\mathrm{F}}(\omega_{\mathrm{mw}} + \omega_{\mathrm{I}}) - P_{\mathrm{S}}(\omega_{\mathrm{mw}})}{1 - P_{\mathrm{S}}(\omega_{\mathrm{mw}}) P_{\mathrm{F}}(\omega_{\mathrm{mw}} + \omega_{\mathrm{I}})}. \qquad \text{Eq. S34}$$

Assuming that fast-relaxing spins are always at Boltzmann polarization P_0 and writing $P_{\mathrm{S}}(\omega_{\mathrm{mw}}) = P^{\mathrm{sat}}$, we have

$$P_{\mathrm{I}}^{\mathrm{tCE,left}}(\omega_{\mathrm{mw}}) = \frac{P^{\mathrm{sat}} - P_0}{1 - P^{\mathrm{sat}} P_0}, \qquad \text{Eq. S35}$$

and

$$P_{\mathrm{I}}^{\mathrm{tCE,right}}(\omega_{\mathrm{mw}}) = \frac{P_0 - P^{\mathrm{sat}}}{1 - P^{\mathrm{sat}} P_0}. \qquad \text{Eq. S36}$$

Hence, the

$$P_{\mathrm{I}}^{\mathrm{tCE}}(\omega_{\mathrm{mw}}) = \frac{f_{\mathrm{S}}(\omega_{\mathrm{mw}})f_{\mathrm{F}}(\omega_{\mathrm{mw}}-\omega_{\mathrm{I}})}{F_{\mathrm{N}}} P_{\mathrm{I}}^{\mathrm{tCE,left}}\left(\omega_{\mathrm{\mu w}}\right) + \frac{f_{\mathrm{S}}(\omega_{\mathrm{mw}})f_{\mathrm{F}}(\omega_{\mathrm{mw}}+\omega_{\mathrm{I}})}{F_{\mathrm{N}}} P_{\mathrm{I}}^{\mathrm{tCE,right}}(\omega_{\mathrm{mw}})$$

$$= \frac{1}{F_{\mathrm{N}}} \frac{P_0 - P^{\mathrm{sat}}}{1-P^{\mathrm{sat}}P_0} f_{\mathrm{S}}(\omega_{\mathrm{mw}})\left(f_{\mathrm{F}}(\omega_{\mathrm{mw}}+\omega_{\mathrm{I}}) - f_{\mathrm{F}}(\omega_{\mathrm{mw}}-\omega_{\mathrm{I}})\right), \qquad \text{Eq. S37}$$

where the normalization factor is defined as

$$F_{\mathrm{N}} = \int d\omega f_{\mathrm{S}}(\omega)\left(f_{\mathrm{F}}(\omega+\omega_{\mathrm{I}}) + f_{\mathrm{F}}(\omega-\omega_{\mathrm{I}})\right). \qquad \text{Eq. S38}$$

The shape of the tCE profile is then given by Eq. S38, dropping constant factors

$$f_{\mathrm{tCE}}\left(\nu_{\mathrm{\mu w}}\right) = f_{\mathrm{S}}(\omega_{\mathrm{mw}})\left(f_{\mathrm{F}}(\omega_{\mathrm{mw}}+\omega_{\mathrm{I}}) - f_{\mathrm{F}}(\omega_{\mathrm{mw}}-\omega_{\mathrm{I}})\right). \qquad \text{Eq. S39}$$

In the case where the fast-relaxing are shifted from the slow-relaxing by approximately ω_{I} (i.e., resonance-matched), only one of the two terms $f_{\mathrm{F}}(\omega_{\mathrm{mw}} + \omega_{\mathrm{I}})$ and $f_{\mathrm{F}}(\omega_{\mathrm{mw}} - \omega_{\mathrm{I}})$ is non-zero. Furthermore, if the resonance of the fast-relaxing spins is broad compared to the slow-relaxing spins, the value of f_{F} in the one term that is non-zero can be considered constant over the range where $f_{\mathrm{S}}(\omega_{\mathrm{mw}})$ is non-zero. Then, we have either

$$f_{\mathrm{tCE}}(\omega_{\mathrm{mw}}) \approx +f_{\mathrm{S}}(\omega_{\mathrm{mw}}), \qquad \text{Eq. S40}$$

or

$$f_{\mathrm{tCE}}(\omega_{\mathrm{mw}}) \approx -f_{\mathrm{S}}(\omega_{\mathrm{mw}}), \qquad \text{Eq. S41}$$

whether the fast-relaxing spins are shifted by $+\omega_{\mathrm{I}}$ or $-\omega_{\mathrm{I}}$ with respect to the EPR line of the slow-relaxing spins, respectively. In this case, the DNP profile has the same shape as the EPR line, up to a sign, as is the case for the Overhauser effect.

d. DNP model including spectral diffusion

To include spectral diffusion in the simulations of the CE and tCE, one must consider the triple flips of the nucleus with all pairs of electrons spins fulfilling the CE matching conditions, not only on resonance with the mm-waves. In the case of the CE, the sum can be written as

$$P_{\mathrm{I}}^{\mathrm{CE}}(\omega_{\mathrm{mw}}) = \frac{1}{F_{\mathrm{n}}} \sum_{k=1}^{N} f(\omega_k) f(\omega_k+\omega_{\mathrm{I}}) \frac{P_{\mathrm{mw}}(\omega_k+\omega_{\mathrm{I}}) - P_{\mathrm{mw}}(\omega_k)}{1-P_{\mathrm{mw}}(\omega_k+\nu_{\mathrm{I}})P_{\mathrm{mw}}(\omega_k)}, \qquad \text{Eq. S42}$$

where *N* is the number of bins in the EPR spectrum, and the normalization factor is

$$F_{\mathrm{n}} = \sum_{k=1}^{N} f(\omega_k) f(\omega_k+\omega_{\mathrm{I}}). \qquad \text{Eq. S43}$$

Note that it is not necessary to account for triple-spin flips on the left and right, as they are both covered by the summation. In the case of the tCE, the integration yields

$$P_{\mathrm{I}}^{\mathrm{tCE}}(\omega_{\mathrm{mw}}) = \frac{1}{F_{\mathrm{n}}} \sum_k \left(f_{\mathrm{S}}(\omega_k) f_{\mathrm{F}}(\omega_k-\omega_{\mathrm{I}}) \frac{P_0 - P_{\mathrm{S}}^{\mathrm{mw}}(\omega_k)}{1-P_0 P_{\mathrm{S}}^{\mathrm{mw}}(\omega_k)} + f_{\mathrm{S}}(\omega_k) f_{\mathrm{F}}(\omega_k+\omega_{\mathrm{I}}) \frac{P_{\mathrm{S}}^{\mathrm{mw}}(\omega_k) - P_0}{1-P_0 P_{\mathrm{S}}^{\mathrm{mw}}(\omega_k)} \right), \qquad \text{Eq. S44}$$

where *N* is the number of bins in the EPR spectrum, and the normalization factor is

$$F_{\mathrm{n}} = \sum_{k=1}^{N} \left(f_{\mathrm{S}}(\omega_k) f_{\mathrm{F}}(\omega_k-\omega_{\mathrm{I}}) + f_{\mathrm{S}}(\omega_k) f_{\mathrm{F}}(\omega_k+\omega_{\mathrm{I}}) \right). \qquad \text{Eq. S45}$$

4. Simulation results

a. P1 EPR line

Figure S7 shows the simulated EPR line at 14.1 T as in the main text of the paper (black line) together with the contributions of the different P1 populations.

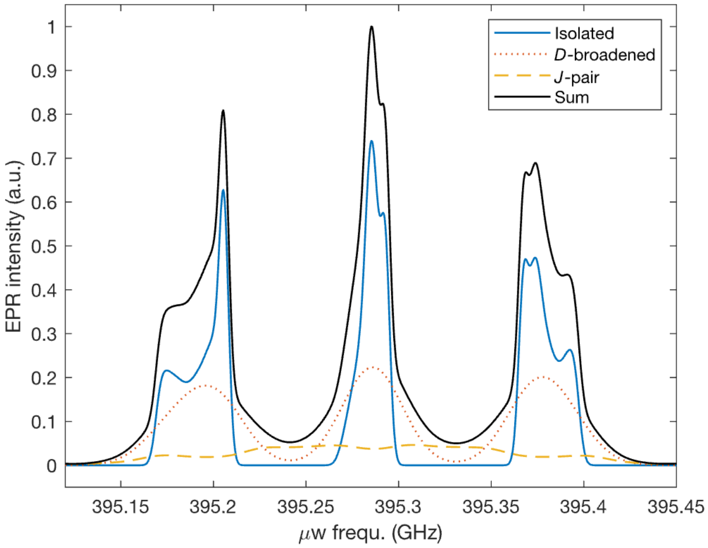

Figure S7: Simulation of the EPR line using *Easyspin's* function *pepper* for solid-state powder averaging. The summed spectrum (in black) is decomposed into three contributions (isolated, dipolar-broadened, and exchange-coupled pairs). See the Methods section for details on the simulation parameters.

b. DNP profiles with different hole burning models

The DNP profiles were simulated for P1 spins at 14.1 T as a linear combination

$$f(\omega_{\mathrm{mw}}) = x_{\mathrm{tCE}} f_{\mathrm{tCE}}(\omega_{\mathrm{mw}}) + (1 - x_{\mathrm{tCE}}) f_{\mathrm{CE}}(\omega_{\mathrm{mw}}), \qquad \text{Eq. S44}$$

where x_{tCE} is contribution of the tCE profile between 0 and 1, using Eqs. S42 and S44. The polarization of the slow-relaxing P1 spins as function of frequency $P_{\mathrm{S}}^{\mathrm{mw}}(\omega_{\mathrm{k}})$ was computed using both hole burning models presented in Section 3b. In both cases, it was assumed that dipolar-broadened and exchange-coupled P1 spins play the role of slow- and fast-relaxing partners. Figure S8 shows the simulated DNP profiles using Vega's eSD model (see Eq. S4) and the analytical solution to the diffusion equation (see Eq. S14), in panel a and b, respectively. For the eSD model, 11 free parameters were manually fit to the experimental data: x_{tCE}, T_1 (individually for set of experimental conditions), T_2, ω_1, and Λ^{eSD}, respectively, (the last three being kept constant for all conditions). For the analytical model, the only fit parameters were x_{tCE} and the spectral diffusion length Λ. Table S2 summarizes the fit results. The digitization of the EPR spectrum was set to a low value for the eSD model (as represented by dots on the EPR lines of the bottom plots of Figure S8a) to fulfill the condition[4] that the frequency difference between the bins (8 MHz) does not exceed the homogeneous broadening: $\omega_{k+1} - \omega_{\mathrm{k}} > 2/T_2$ (8 MHz). In the case of the analytical model, there is requirement regarding the frequency separation between the bins.

Table S2: Fit parameters of the spectral diffusion/hole burning models used to compute the DNP profiles shown in Figure S8.

Vega's eSD model				
T (K)	298, Static	298, MAS	100	35
x_{tCE}	0.5	0.5	0.5	0.5
T_1 (ms)	0.12	0.12	4	5
T_2 (ns)	40			
$\omega_1/2\pi$ (kHz)	300			
Λ^{eSD} (μs^{-3})	800			

Analytical model				
T (K)	298, Static	298, MAS	100	35
x_{tCE}	0.6	0.6	0.7	0.7
Λ (MHz)	22	20	130	130

a. Using Vega's eSD model

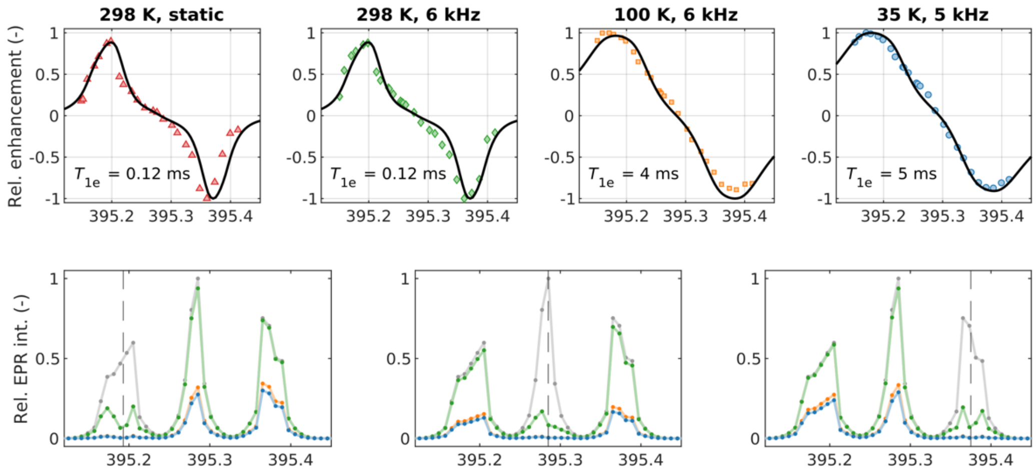

b. Using analytical solution to the spectral diffusion equation

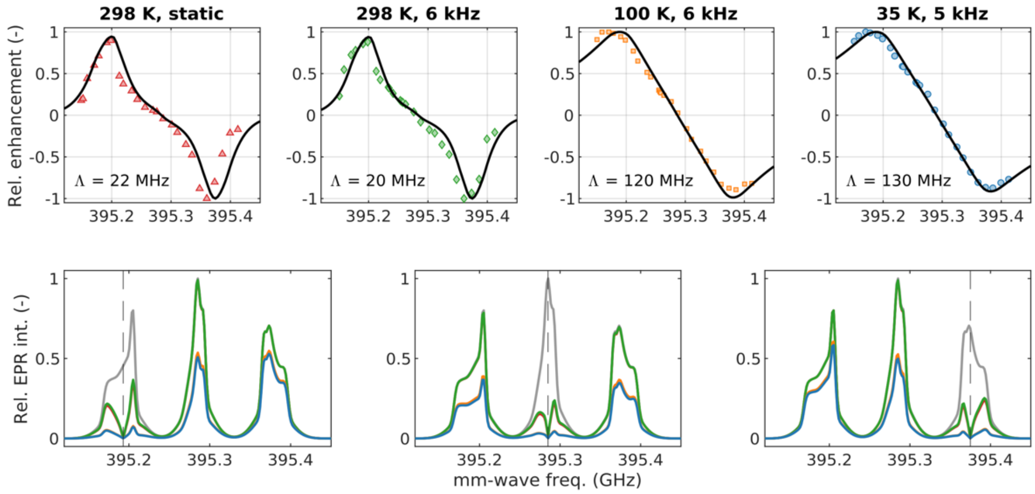

Figure S8: Computation of the simulated DNP profiles using Eqs. S42 and S44 and the Vega's eSD model (see Eq. S4) and the analytical solution to the diffusion equation (see Eq. S14), panel a and b, respectively. In each panel, the top row represents the normalized experimental DNP profiles (colored symbols) and the model (black lines). The bottom row represents the EPR line of the slow-relaxing spins under saturation (colored lines) compared with that at thermal equilibrium (grey lines), for three different mm-wave frequencies (represented by vertical dashed lines).

Table S3: Separation between the positive and negative DNP optima in the experimental profiles Δ_{exp}, compared with that of the simulated profiles Δ_{sim} (simulated using the analytical solution to the diffusion equation), and the profiles of the tCE and CE contributions, Δ_{tCE} and Δ_{CE}, respectively, for the simulation using the analytical solution to the diffusion equation.

T (K)	Δ_{exp}	Δ_{sim}	Δ_{tCE}	Δ_{CE}
298, static	162	175	188	150
298, MAS	162	175	184	150
100	215	188	196	163
35	215	196	196	163

c. *SE-DNP simulation*

Figure S9 shows the simulated DNP profile for the SE (in gray) using Eq. S19 and the entire EPR line (isolated, dipolar-broadened, and exchange-coupled spins) compared with the experimental results in all experimental conditions (colored symbols).

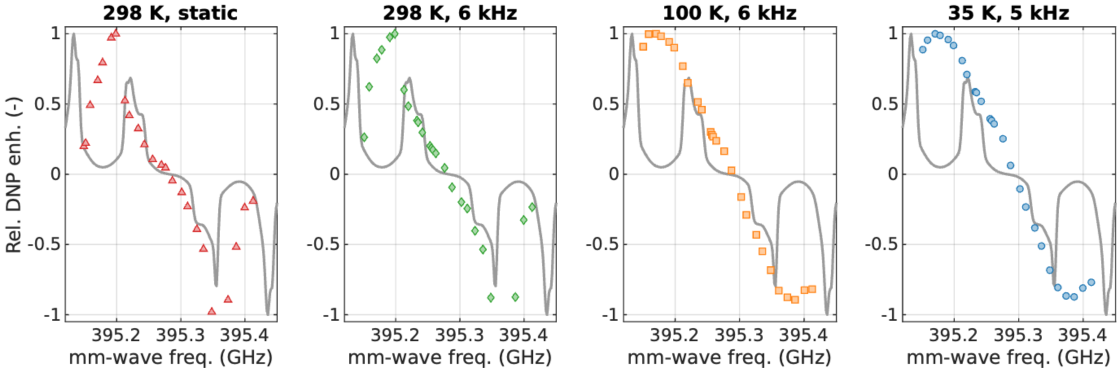

Figure S9: SE simulation using Eq. S19 (gray line), compared with the experimental data (colored dots).

d. *Prediction of the DNP profiles at 3.3 and 6.9 T*

The ^{13}C-DNP profiles acquired at 3.3 and 6.9 T and room temperature for the same diamond sample were reported in Ref. [12]. It is shown in Figure S10 as red triangles. We applied the model shown Figure 6, that is, CE and tCE where spectral diffusion is computed using the analytical expression of Eq. 3. In these conditions (lower field and possibly stronger saturating field), the contribution of the SE is more pronounced than at 14.1 T, so it was included in the simulation. The black lines show the individual simulated DNP profiles and their sum. The EPR line of the slow relaxing spins (dipolar-broadened and isolated) at thermal equilibrium and under saturation at a select frequency (grey and lines, respectively) is shown in the top right plot of each panel. The EPR line of the fast-relaxing spins (exchange-coupled pairs) is shown in the bottom right plot of each panel. The spectral diffusion length and relative contributions of the tCE, CE, and SE were manually fitted. The static magnetic field of 3.3476 and 6.9074 T were also let free to align the simulated and experimental profiles. The spectral diffusion length was fitted to 6 and 22 MHz at 3.3 and 6.9 T, respectively. For comparison, a spectral diffusion length of 22 MHz was obtained at 14.1 T (see Table S2).

The model is in good agreement with the experimental data at 6.9 T (see Figure S10b). At 3.3 T, the model reproduces most of the features (see Figure S10a). However, the central negative absorptive feature is not reproduced by the model (highlighted in yellow in Figure S10a). This very feature was attributed to tCE by Bussandri *et al*.[12] It is possible that the fast-relaxing spins taking part into the proposed tCE feature are spin species different from P1 centers, as suggested by Bussandri *et al*.[12]

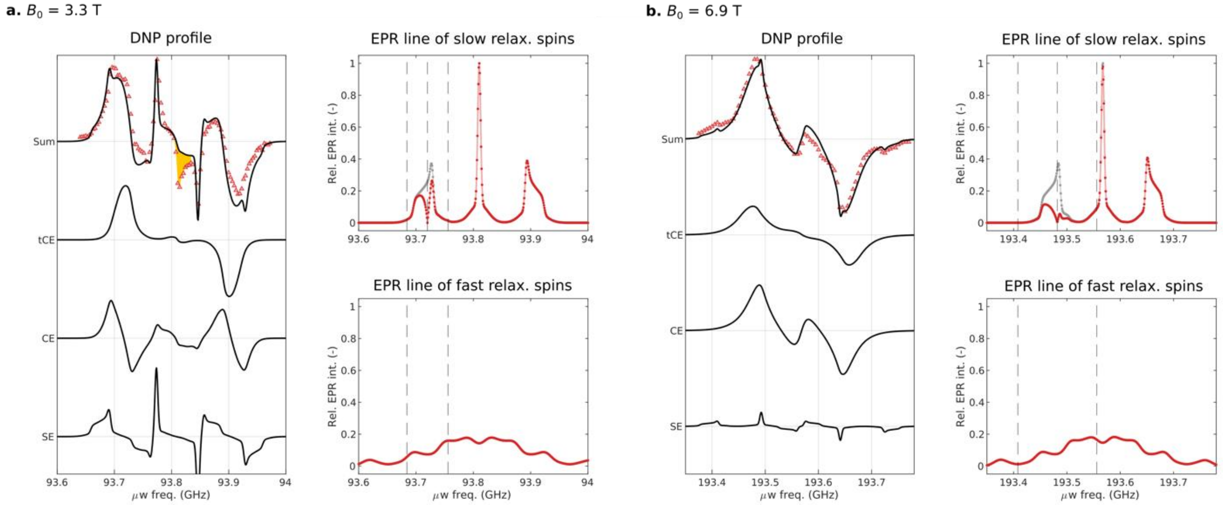

Figure S10: **a,b**. Comparison of the experimental DNP profiles reported in Ref. [12] at 3.3 and 6.9 T, respectively, and room temperature in static mode for the same diamond sample as in this study. The top plots on the right of each panel show the EPR line of the slow-relaxing spins at thermal equilibrium and under saturation at a select frequency, represented as grey and red lines, respectively. The black dashed lines represent the microwave irradiation frequency and the two corresponding positions for triple-spin flips partners. The bottom plots on the right of each panel show the EPR line of the fast-relaxing spins at thermal equilibrium. The black dashed lines represent the two positions for triple-spin that correspond to the irradiation frequency on the plot of the slow-relaxing spins. The yellow area in panel a highlights the region where the model does not reproduce the experimental data.

e. Transition distribution for exchange-coupled P1 pairs

The EPR spectrum of the exchange-coupled was simulated using EasySpin function *pepper*, with the option that separates the EPR spectrum into the components corresponding to different transitions (option *separate* set to the value *transitions*) for a magnetic field of 14.1 T and using the parameters given in the Methods section of the paper. The resulting spectra are shown in the left panel of Figure S11 (as colored lines). The sum of all the components corresponds to the whole EPR line and is shown as a black line. The transition intensities were calculated by integrating the individual components. Their relative contributions of the transitions are shown on the right panel of Figure S11 as blue dots, ordered in descending intensity. The cumulative distribution of the blue curve in Figure S11 is shown in black on the same plot. This plot shows that the most intense transition only contributes to about 5% of the total EPR line and the 20 first most intense transitions account for less than 50% of the total EPR line.

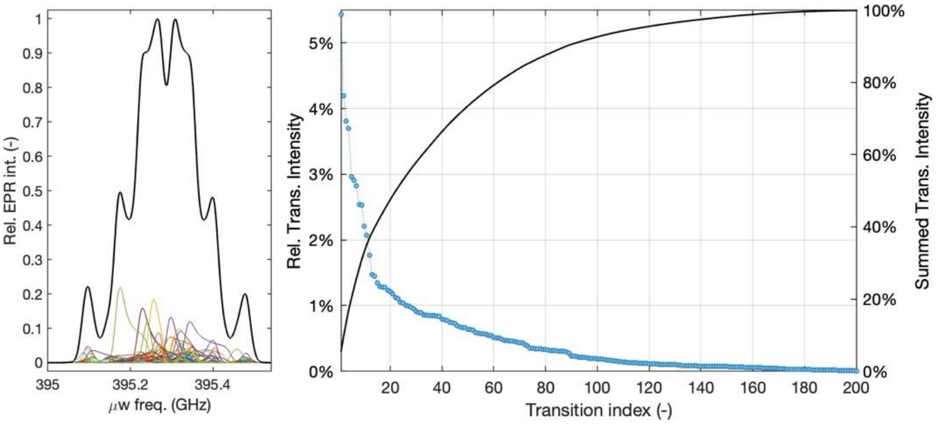

Figure S11: Decomposition into individual transitions of the powder-averaged EPR spectrum of exchange-coupled P1 spin pairs. Left: EPR spectrum of the individual transitions (colored lines) and sum of all transitions (black line). Right: Transition intensities (obtained by integrating the spectra on the left) ordered from most to least intense (blue dots) and cumulative distribution of the transition intensities (black line).

References

(1) Li, Y.; Chaklashiya, R.; Takahashi, H.; Kawahara, Y.; Tagami, K.; Tobar, C.; Han, S. Solid-State MAS NMR at Ultra Low Temperature of Hydrated Alanine Doped with DNP Radicals. *J. Magn. Reson.* **2021**, *333*, 107090. https://doi.org/10.1016/j.jmr.2021.107090.

(2) Nir-Arad, O.; Shlomi, D. H.; Israelstam, A.; Amit, T.; Manukovsky, N.; Fialkov, A. B.; Kaminker, I. The CW-EPR Capabilities of a Dual DNP/EPR Spectrometer Operating at 14 and 7 T. *J. Magn. Reson.* **2024**, *360*, 107635. https://doi.org/10.1016/j.jmr.2024.107635.

(3) Nir-Arad, O.; Fialkov, A. B.; Shlomi, D. H.; Manukovsky, N.; Mentink-Vigier, F.; Kaminker, I. High-Field Pulsed EPR Spectroscopy under Magic Angle Spinning. *Sci. Adv.* **2024**, *10* (35), eadq6073. https://doi.org/10.1126/sciadv.adq6073.

(4) Hovav, Y.; Kaminker, I.; Shimon, D.; Feintuch, A.; Goldfarb, D.; Vega, S. The Electron Depolarization during Dynamic Nuclear Polarization: Measurements and Simulations. *Phys. Chem. Chem. Phys.* **2015**, *17* (1), 226–244. https://doi.org/10.1039/C4CP03825H.

(5) Kundu, K.; Cohen, M. R.; Feintuch, A.; Goldfarb, D.; Vega, S. Experimental Quantification of Electron Spectral-Diffusion under Static DNP Conditions. *Phys. Chem. Chem. Phys.* **2019**, *21* (1), 478–489. https://doi.org/10.1039/C8CP05930F.

(6) Wenckebach, W. Th. Spectral Diffusion of Electron Spin Polarization in Glasses Doped with Radicals for DNP. *J. Magn. Reson.* **2024**, *360*, 107651. https://doi.org/10.1016/j.jmr.2024.107651.

(7) Kundu, K.; Feintuch, A.; Vega, S. Electron–Electron Cross-Relaxation and Spectral Diffusion during Dynamic Nuclear Polarization Experiments on Solids. *J. Phys. Chem. Lett.* **2018**, *9* (7), 1793–1802. https://doi.org/10.1021/acs.jpclett.8b00090.

(8) Kundu, K.; Mentink-Vigier, F.; Feintuch, A.; Vega, S. DNP Mechanisms. *Handb. High Field Dyn. Nucl. Polariz.* **2019**, 15.

(9) Vaneeckhaute, E.; Bocquelet, C.; Rougier, N.; Jegadeesan, S. A.; Vinod-Kumar, S.; Mathies, G.; Melzi, R.; Kempf, J.; Stern, Q.; Jannin, S. Dynamic Nuclear Polarization Mechanisms Using TEMPOL and Trityl OX063 Radicals at 1 T and 77 K. 2024. https://doi.org/10.48550/arXiv.2412.10325.

(10) Kundu, K.; Feintuch, A.; Vega, S. Theoretical Aspects of the Cross Effect Enhancement of Nuclear Polarization under Static Dynamic Nuclear Polarization Conditions. *J. Phys. Chem. Lett.* **2019**, *10* (8), 1769–1778. https://doi.org/10.1021/acs.jpclett.8b03615.

(11) Wenckebach, W. T. Dynamic Nuclear Polarization via the Cross Effect and Thermal Mixing: A. The Role of Triple Spin Flips. *J. Magn. Reson.* **2019**, *299*, 124–134.

(12) Bussandri, S.; Shimon, D.; Equbal, A.; Ren, Y.; Takahashi, S.; Ramanathan, C.; Han, S. P1 Center Electron Spin Clusters Are Prevalent in Type Ib Diamonds. *J. Am. Chem. Soc.* **2023**, jacs.3c06705. https://doi.org/10.1021/jacs.3c06705.